Focused Connected Array Antenna as a Broadband Beam-Steering Feed for Quasi-Optical System

Pascual Laguna, Alejandro; Cavallo, Daniele; Baselmans, Jochem J.A.; Llombart, Nuria

DOI
10.1109/TAP.2022.3142291

Publication date
2022

Document Version
Accepted author manuscript

Published in
IEEE Transactions on Antennas and Propagation

Communication

Focused Connected Array Antenna as a Broadband Beam-Steering Feed for Quasi-Optical Systems

Alejandro Pascual Laguna, Daniele Cavallo, Jochem J. A. Baselmans, and Nuria Llombart

***Abstract*—This paper proposes a broadband and efficient integrated focal plane array solution based on a near-field focused connected array of slots. The focused aperture provides (1) broadband and highly efficient illumination of the quasi-optical system, and (2) scanning capabilities within a focusing system. The connected array antenna in turn allows for a fully integrated solution that can synthesize a focused aperture while providing broadband impedance matching. Focused connected array antennas enable the coupling to a reflector system over bandwidths in excess of one octave and with aperture efficiencies in excess of 60%. To demonstrate the concept we present two printed circuit board (PCB) prototypes operating in the band 3–6 GHz and yielding more than 60% reflector aperture efficiency under broadside illumination and allowing to scan one beamwidth at the lowest frequency with a frequency-averaged scan loss of 0.2 dB. The feasibility of scaling this concept to THz frequencies and with dynamic beam-steering capabilities is discussed in the context of a superconducting device.**

***Index Terms*—aperture efficiency, broadband array, connected array, focused aperture, near-field, scanning.**

I. INTRODUCTION

BROADBAND illumination of quasi-optical systems with high aperture efficiency is desired for wideband instruments. This is typically achieved with electrically large feeds that, when used in imaging arrays, require beam scanning capabilities for the full coverage of the field of view. One application of such systems is in terahertz (THz) broadband on-chip superconducting spectrometers for astronomy.

Reflector feeds synthesizing frequency-stable beams have been demonstrated in the literature, specially in the microwave regime. There exist successful examples based on lens antennas [1]–[4], log-periodic antennas [5], [6] and horn antennas [7]–[10]. All the mentioned works achieved low dispersive beams over a bandwidth of at least one octave.

In the THz regime there are fewer examples in the literature for frequency-independent feeds. The predominant technology is the corrugated horn [11]. Recently, an integrated hyper-hemispherical leaky lens antenna has been proposed as an on-chip antenna solution [12] requiring a broadband anti-reflection (AR) coating for the silicon lens. However, such broadband AR-coatings are difficult to fabricate with stable mechanical properties at cryogenic temperatures. To provide directive beams, without requiring the use of integrated lenses, phased-array antennas based on superconducting corporate feeding networks have been used [13]–[15]. These superconducting transmission lines have been demonstrated to have negligible losses at THz frequencies [16], [17], enabling efficient phased-array feeding networks.

In this work we propose a broadband antenna array concept as a reflector feed in an out-of-focus phased-array configuration within a reflector system such as [18]–[20]. The feed consists of a connected array of slots focusing in the near field [21]. Unlike narrowband focused aperture concepts [22]–[24], the proposed solution can operate over bands larger than one octave and with scanning capabilities. Two prototype antennas based on printed circuit board (PCB) technology in the band 3–6 GHz are realized, one scanning broadside and another scanning one beam at the lowest frequency.

The presented concept has potential to be implemented as a superconducting phased-array at THz frequencies with electronic beam-steering, by means of phase-shifters based on the tunable superconducting delay lines [25]. The fabrication at THz frequencies is now within reach with the technology developed in [26], [27].

II. NEAR-FIELD FOCUSED APERTURE

A circular aperture of diameter D with a uniform amplitude and a constant phase, henceforth called an unfocused[1] aperture following Sherman's terminology [28], produces far fields proportional to the Airy pattern. The far-field half-power beamwidth (HPBW) of this aperture is dispersive and it is given by λ/D radians, where λ is the wavelength. Focused apertures exhibit similar properties such as frequency dispersion of the beamwidth, but in the near field (Fresnel region) instead of the far field [28], [29]. In this section we will investigate these properties and how they can be exploited to render a broadband, efficient and steerable feeder for a focusing system.

Manuscript received April 9, 2021; revised October 22, 2021; accepted December 25, 2021. Date of publication Month dd, yyyy; date of current version December 25, 2021. This work was supported by the European Research Council Consolidator Grant (ERC-2014-CoG MOSAIC), no. 648135 and by the European Research Council Consolidator Grant (ERC-2014-StG LAA-THz-CC), no. 639749. (*Corresponding author: A. Pascual Laguna.*)

A. Pascual Laguna, D. Cavallo, J. J. A. Baselmans, and N. Llombart are with the THz Sensing group, Microelectronics Department, Delft University of Technology, 2628 CD Delft, The Netherlands (e-mail: A.Pascual.Laguna@sron.nl).

A. Pascual Laguna and J. J. A. Baselmans are also with SRON Netherlands Institute for Space Research, 2333 CA Leiden, The Netherlands.

Color versions of one or more of the figures in this paper are available online at https://ieeexplore.ieee.org.

Digital Object Identifier xx.xxxx/TAP.xxxx.xxxxxxx

[1] An unfocused aperture is actually focused at infinity.

This article has been accepted for publication in a future issue of this journal, but has not been fully edited. Content may change prior to final publication. Citation information: DOI 10.1109/TAP.2022.3142291, IEEE Transactions on Antennas and Propagation

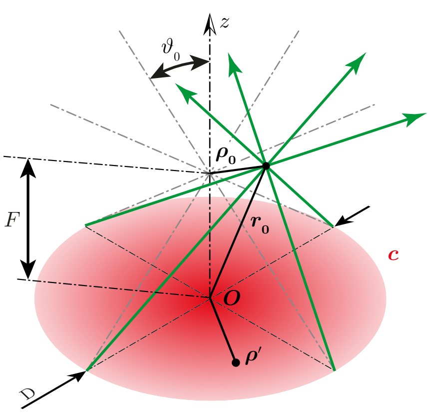

Fig. 1. A focused circular aperture of diameter D. ϑ_0 is the de-focusing angle subtended between the normal of the aperture and the ray emerging from the edge of the aperture and passing through the focus at a focal distance F.

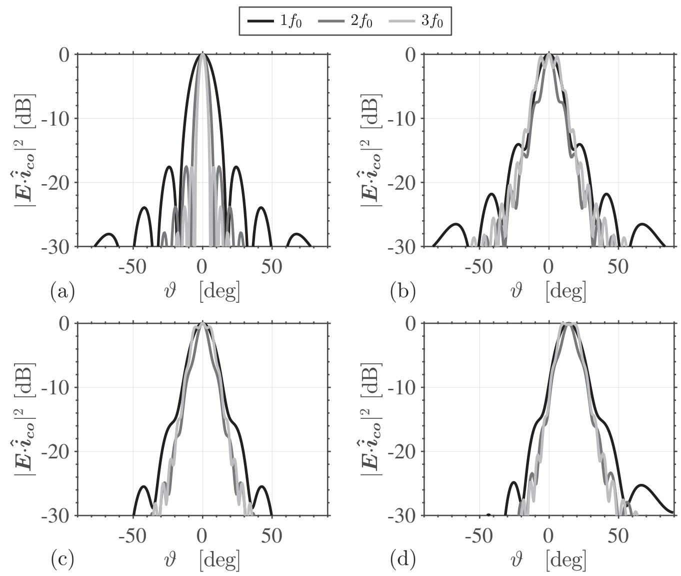

Fig. 2. Normalized co-polarized component of the E-plane electric far-field patterns of a circular aperture with $D = 4\lambda_0$, where λ_0 is the wavelength at the lowest frequency f_0, for: (a) a conventional unfocused aperture and an $f_{\#} = 2$ focused aperture (b) with a uniform amplitude, (c) with a Gaussian amplitude taper characterized by $T_{\text{edge}}|_{\text{dB}} = -7$, and (d) with the same taper while scanning one HPBW ($\rho_0 = \lambda f_{\#}$) in the focal plane, or equivalently to $\vartheta \approx 14.3°$ in the far field.

A. Focusing Currents

Let us consider a current distribution on a circular aperture of diameter D, whose center coincides with the origin of the reference system as sketched in Fig. 1. The currents are such that radiation focuses at the point $\boldsymbol{r_0} = (x_0, y_0, F)$ in the plane $z = F$. Their expression is written out in terms of their location $\boldsymbol{\rho'} = (x', y', 0)$ as

$$\boldsymbol{c}(\boldsymbol{\rho'}) = e^{jk|\boldsymbol{r_0}-\boldsymbol{\rho'}|} e^{-\frac{1}{w_0^2}\rho'^2} \operatorname{circ}(\rho'; D/2)\hat{\boldsymbol{c}}, \tag{1}$$

where $\rho' = |\boldsymbol{\rho'}| = (x'^2+y'^2)^{1/2}$ is the radial component of the position of the currents in cylindrical coordinates, k is the free-space propagation constant, F is the focal distance measured orthogonally from the aperture, $\hat{\boldsymbol{c}}$ is the polarization unit vector and $\operatorname{circ}(\rho'; D/2)$ equals 1 for $\rho' \leq D/2$ and 0 elsewhere. The first exponential term compensates for the phase shift in propagating from a point $\boldsymbol{\rho'}$ in the aperture to the point $\boldsymbol{r_0}$. The second exponential term provides a Gaussian amplitude taper whose waist w_0 is fixed for certain edge taper in dB $T_{\text{edge}}|_{\text{dB}}$ (defined negative) as $w_0 = (-5D^2 \log_{10}(e)/T_{\text{edge}}|_{\text{dB}})^{1/2}$. The current in (1) can then be approximated for flash points $\boldsymbol{r_0}$ in the proximity of $(0, 0, F)$ as

$$\boldsymbol{c}(\boldsymbol{\rho'}) \approx e^{j\frac{k}{2F}\rho'^2} e^{-j\frac{k}{F}(x_0x'+y_0y')} e^{-\frac{1}{w_0^2}\rho'^2} \operatorname{circ}(\rho'; D/2)\hat{\boldsymbol{c}}, \tag{2}$$

when $|\boldsymbol{\rho_0} - \boldsymbol{\rho'}| \ll F$, being $\boldsymbol{\rho_0} = (x_0, y_0, 0)$ the radial vector to the flash point in the focal plane [28]. The first exponential term in (2) is a quadratic phase shift providing the focusing and the second a linear phase shift to scan the flash point $\boldsymbol{r_0}$ in the focal plane.

Thanks to the beamwidth dispersion in the near field, the far fields of focused apertures have fairly frequency-independent beam-widths when compared to unfocused apertures as can be seen from Fig. 2(a) and 2(b). Furthermore, the diffraction given by the finite size of the focused aperture also causes far-field ripples, which can be attenuated with an amplitude taper as exemplified in Fig. 2(c). Lastly, Fig. 2(d) shows a steered far-field beam due to the displacement of the flash-point in the focal plane as depicted in Fig. 1. It is apparent that a focused aperture broadens the far-field beamwidth due to the diverging rays beyond the focus. As a result, the beamwidth is proportional to the de-focusing angle $\vartheta_0 = \operatorname{atan}(1/(2f_{\#}))$, which depends on the focal ratio $f_{\#} = F/D$. The phase center of the focused aperture far fields is at the flash point.

B. Broadband and Highly-Efficient Quasi-Optical Coupling

To quantify the illumination efficiency, the simplified quasi-optical system in Fig. 3 is investigated. For a non-scanning scenario, it chiefly consists of a confocal parabolic reflector sharing the focal ratio $f_{\#}$ with the focused aperture, but with magnification D_{refl}/D, where D_{refl} is the diameter of the parabolic reflector. For this analysis, the current in (2) is propagated to the near-field focal plane with the free-space radiation integral, and subsequently propagated with GRASP to a parabolic reflector using Physical Optics. In this procedure, the spill-over efficiency η_{so} is calculated by the software. The taper efficiency η_{tap} is calculated from the ratio between the achieved directivity and the maximum theoretical directivity $D_{\max} = 4\pi A/\lambda^2$, where A is the reflector cross-section. The reflector aperture efficiency is $\eta_{\text{ap}} = \eta_{\text{tap}} \cdot \eta_{\text{so}}$.

As shown in Fig. 4, the aperture efficiency η_{ap} of a reflector illuminated by an unfocused aperture peaks around $D = 2\lambda f_{\#}$. On the contrary, η_{ap} for the focused aperture is relatively flat for $D/(\lambda f_{\#}) \geq 2$. Different amplitude tapers are also shown in Fig. 4. An edge taper of $T_{\text{edge}}|_{\text{dB}} = -7$ is chosen, as larger values do not give further improvement.

C. Scanning Capabilities Inside a Focusing System

To enable scanning inside a focusing system, a small off-focus shift has to be introduced in the focal plane, which corresponds to a linear phase-shift in the primary fields illuminating a quasi-optical system, and eventually a beam tilt

This article has been accepted for publication in a future issue of this journal, but has not been fully edited. Content may change prior to final publication. Citation information: DOI 10.1109/TAP.2022.3142291, IEEE Transactions on Antennas and Propagation

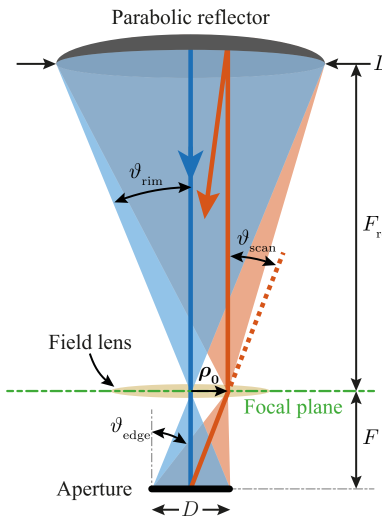

Fig. 3. Focused aperture illuminating a reflector system. A field lens is placed at the focal plane to collimate the scanned beams.

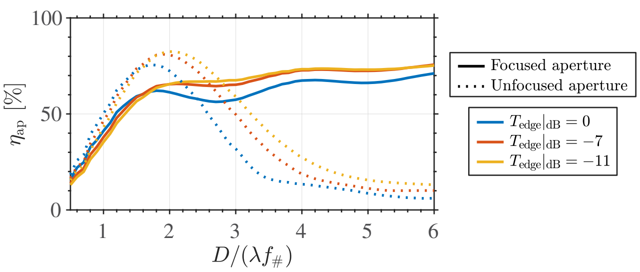

Fig. 4. Reflector aperture efficiency as a function of the feeding aperture size for focused and unfocused circular apertures and for different aperture tapers.

in the secondary fields radiated by the reflector [30]. This is illustrated in the simplified quasi-optical system of Fig. 3. To minimize the spill-over losses, a field lens at the focal plane is required to render a telecentric system, where the central ray for each scanned beam comes out parallel to the optical axis.

A real field lens is not included in the simulations, but its ideal effect is accounted for by phase-shifting the focal fields around the flash point $\mathbf{r_0}$ by multiplying them with the term $e^{-jk\sin(-\vartheta_{\text{scan}})((x-x_0)\cos(\varphi_{\text{scan}})+(y-y_0)\sin(\varphi_{\text{scan}}))}$, where $\vartheta_{\text{scan}} = \text{atan}(\rho_0/F)$ and $\varphi_{\text{scan}} = \text{atan}(y_0/x_0)$. Fig. 5(a) showcases the scanning capabilities for both the currents in (1) and (2) for $f_\# = 2$ and $D = 4\lambda_0$, where λ_0 is the wavelength at f_0. As expected, the approximated phase in (2) hampers the scanning performance. Nonetheless, the reflector aperture efficiency is in excess of 60% for at least an octave bandwidth when pointing broadside and scanning one beam at the lowest frequency ($\rho_0 = 1\lambda_0 f_\#$) as reported in Fig. 5(b).

D. Prototype Dimensioning

For the same aperture size D, a smaller focal ratio $f_\#$ is beneficial for the reflector aperture efficiency due to the shrinkage of the depth of focus (-3 dB axial beamwidth) and of the focal spot width. When the beam waist in the near field is comparable to D, the aperture does not focus well anymore and behaves as a standard unfocused aperture.

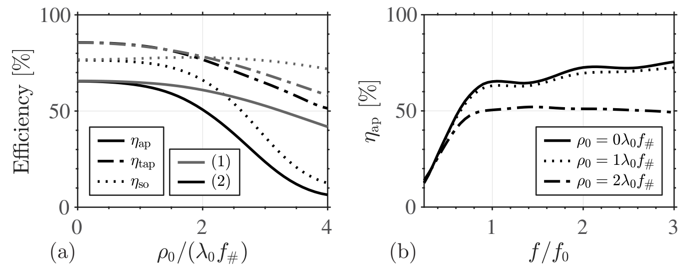

Fig. 5. Quasi-optical efficiencies for scanning scenarios using a focused aperture with a diameter $D = 4\lambda_0$ and $f_\# = 2$. Sub-figure (a) shows the scanning capabilities at f_0 for the currents in (1) and (2) as a function of the radial scanning ρ_0 in the focal plane. Sub-figure (b) shows the aperture efficiency versus frequency for broadside and scanning to one HPBW at f_0 using the currents in (2).

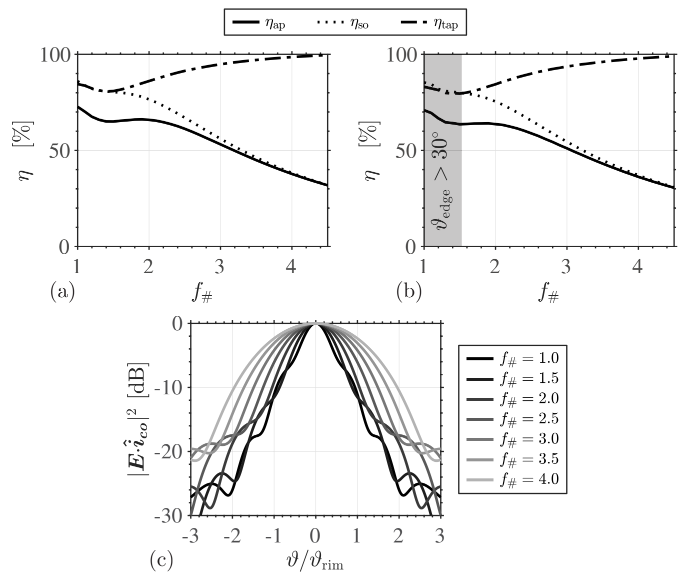

Fig. 6. Efficiencies of the quasi-optical system in Fig. 3 as a function the focal ratio $f_\#$ for a feeding focused aperture with a diameter of $D = 4\lambda$ when (a) pointing broadside and (b) scanning $\rho_0 = 1\lambda f_\#$. Sub-figure (c) shows the far fields of a $D = 4\lambda$ aperture as a function of the angle normalized to the corresponding ϑ_{rim} to emphasize the larger spill over losses for large $f_\#$.

For increasing values of $f_\#$, the subtended angle of the reflector ϑ_{rim} decreases, while the array beamwidth cannot be reduced beyond the diffraction limit, causing spillover losses. This is exemplified in Fig. 6 for $D = 4\lambda$. Moreover, a smaller $f_\#$ is advantageous in that it makes a more compact quasi-optical system. On the other hand, a smaller $f_\#$ enforces a larger scanning angle from the aperture edge, which is given by $\vartheta_{\text{edge}} = \text{atan}((D/2 + \rho_0)/F)$. As we shall see in the next section, a practical implementation of the focused aperture using flat phased-array antennas limits this angle to about 30°, and thereby sets a lower bound for the focal ratio of $f_\#^{\text{min}} = (D/2 + \rho_0)/(D\tan(\vartheta_{\text{edge}}))$. To demonstrate the concept of a beam-steering focused aperture we investigate the scanning of one HPBW ($\rho_0 = 1\lambda f_\#$), for which $f_\#^{\text{min}} \approx 1.527$. Although a larger aperture would allow scanning further and a better illumination of the reflector system, to ease the fabrication of a scaled prototype in standard PCB technology we have fixed $f_\# = 2$ and $D = 4\lambda_0$.

This article has been accepted for publication in a future issue of this journal, but has not been fully edited. Content may change prior to final publication. Citation information: DOI 10.1109/TAP.2022.3142291, IEEE Transactions on Antennas and Propagation

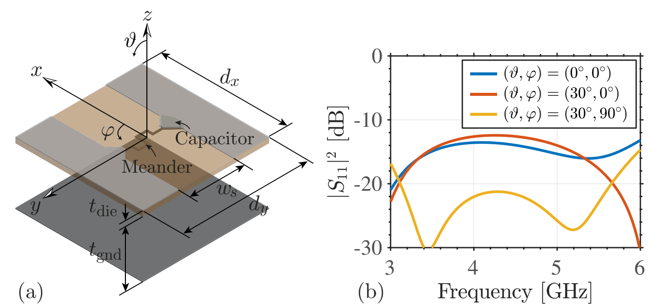

Fig. 7. (a) Unit cell of a y-polarized connected array of slots with its main geometrical parameters. (b) Active reflection coefficient of the unit cell.

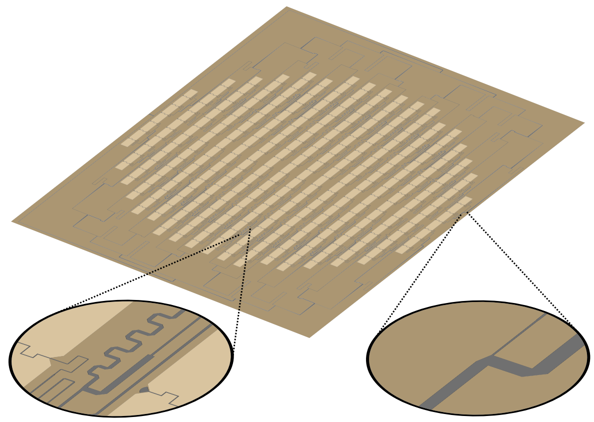

Fig. 8. Circular connected array of slots fed with a corporate feeding network.

III. Focused Connected Array of Slots

A connected array antenna [31] can be used to approximate the currents in (2) over a wide band. Here we employ connected slot elements fed by microstrip lines.

A. Array Unit Cell

Fig. 7 depicts a connected slot unit cell located on an electrically thin dielectric slab, which provides the support for a microstrip feed, without supporting surface waves. The dielectric slab is made with Rogers RT/duroid® 5880 (with relative permittivity $\varepsilon_r \approx 2.2$). Furthermore, a metal plane is located at a distance behind the antenna plane to ensure unidirectional radiation. To counteract the inductive effect on the input impedance of the back reflector, a series capacitor is added at the end of the feeding line as in [32].

The main geometrical parameters, depicted in Fig. 7, are tuned for a design in the band 3–6 GHz scanning up to $\vartheta = 30°$ in all azimuthal planes. The selected values are $d_x = d_y = 21.98\,\mathrm{mm}$, $w_s = 9.49\,\mathrm{mm}$, $t_{\mathrm{die}} = 381\,\mu\mathrm{m}$, $t_{\mathrm{gnd}} = 12.24\,\mathrm{mm}$. The active reflection coefficient of the unit cell, including a $100\,\mu\mathrm{m}$-wide feeding microstrip, are simulated in CST Microwave Studio and shown in Fig. 7 to be matched over an octave.

B. Corporate Feeding Network

The corporate feeding network depicted in Fig. 8 is designed to approximate the currents in (2) for $T_{\mathrm{edge}}|_{\mathrm{dB}} = -7$ and $f_\# = 2$ in the band 3–6 GHz with 256 feeds distributed on a square lattice over a circular aperture. Two feeding networks have been designed, one for the broadside and one for the scanning scenario, respectively. The quadratic and linear phase shifts have been distributed with true-time delay lines in the different stages of the feeding network (inset on the left in Fig. 8) and the amplitude taper has been implemented by means of unbalanced T-junctions (inset on the right in Fig. 8). Moreover, several tapered lines and quarter-wavelength transformers have been used to achieve the required bandwidth and to avoid very wide microstrips. Fig. 9 shows the amplitude and phase aperture distributions of the ideal currents in (2) and of the outputs of the feeding network at 4.5 GHz, simulated in Ansys HFSS and loaded with the unit cell active input impedance. The simulated distribution differs with respect to the ideal profile due to the non-ideal power splitters and impedance transformers in the feeding network, as well as by the cross-talk between microstrip lines. The quasi-optical efficiencies achieved with the simulated feeding network and with the ideal weights show a good agreement in Fig. 10.

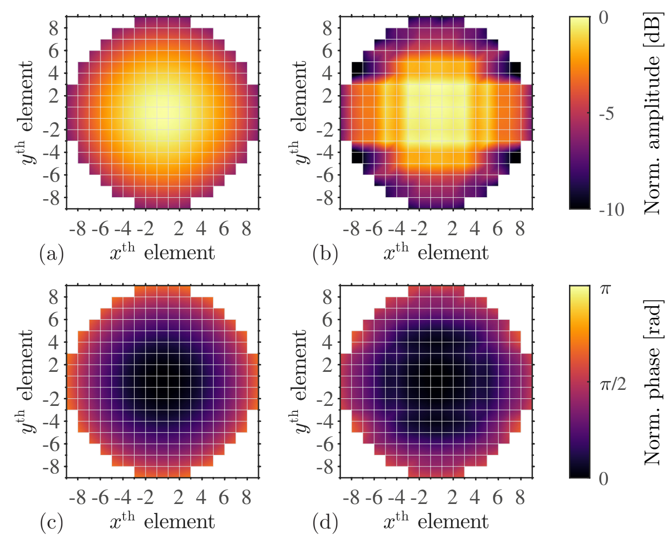

Fig. 9. Feeding network ideal weights, in amplitude (a) and phase (c), using equation (2) and the simulated results from the actual design, in amplitude (b) and phase (d), at 4.5 GHz and pointing broadside.

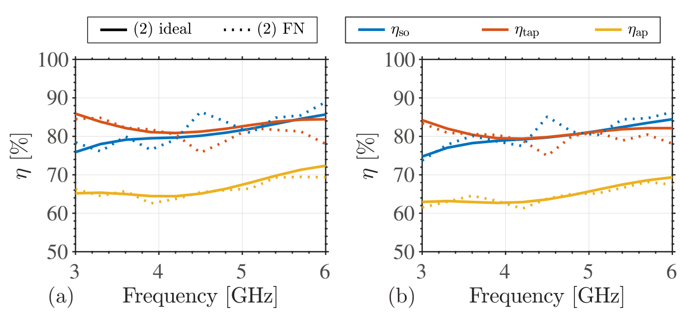

Fig. 10. Comparison of the reflector aperture efficiency, for the (a) broadside and (b) scanning scenarios, when the reflector is fed with the aperture currents in (2), using either the ideal weights for $T_{\mathrm{edge}}|_{\mathrm{dB}} = -7$ and focal ratio $f_\# = 2$ or the simulated weights obtained with the feeding network (FN).

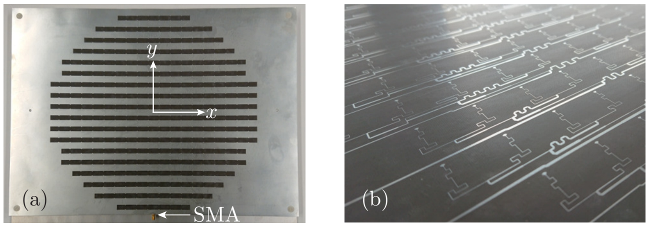

Fig. 11. One of the fabricated prototypes: (a) front side and (b) back side.

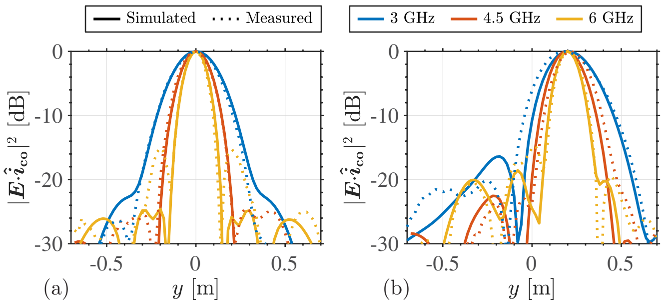

Fig. 12. Simulated and probe-compensated measured E-plane near-field patterns at several frequencies in the focal plane for (a) the array scanning broadside and (b) the array scanning one 3-GHz HPBW in the E-plane.

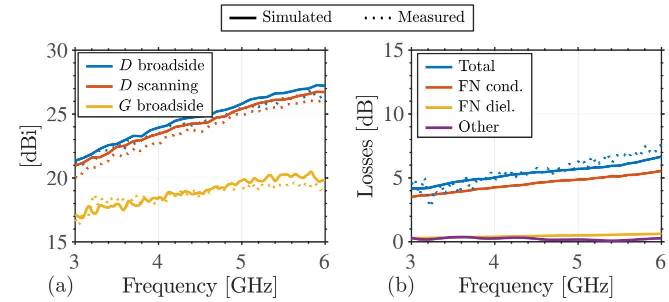

Fig. 13. Sub-figure (a) compiles the simulated and measured (after probe de-embedding) near-field directivity and gain for the antennas pointing broadside and scanning. Sub-figure (b) compares the measured and simulated loss.

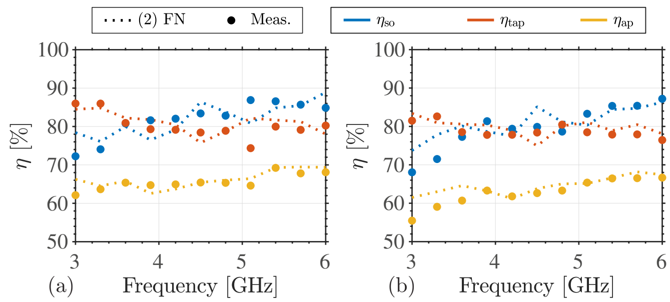

Fig. 14. Comparison of reflector aperture efficiency from simulated and measured patterns, for the (a) broadside and (b) scanning scenarios.

IV. Measurements

Two prototypes of the same antenna array have been fabricated (Fig. 11), differing only in their feeding network: one pointing broadside and another scanning to $1\lambda_0 f_{\#}$ in the focal plane along the E-plane. The E-plane represents the worst scanning plane due to the TM_0 parallel-plate waveguide mode propagation between the back reflector and the slot plane.

Both measured antennas are well matched at the SMA input of the feeding network with a reflection level below -15 dB for the 3–6 GHz band. Fig. 12 compares the measured near-field patterns in the focal plane with the calculated ones using the equivalent current in (2) with the simulated weights in Fig. 9. Probe compensation has been applied [33] to remove the cross-polarization effects of the near-field probe. The simulated beams are in agreement with the measured ones in terms of beamwidth and pointing.

The fields in Fig. 12 are locally a plane wave around the focus, and thus the near-field directivity can be calculated as described in [34]. The near-field directivities depicted in Fig. 13 as a function of frequency agree well with the simulations and show a typical far-field dispersion in the near field. The measured near-field scan loss for the steering antenna averages 0.6 dB in the operational band.

The gain of the array pointing broadside, reported in Fig. 13(a), highlights a large loss, which is detailed separately in Fig. 13(b). Surface-wave and mismatch loss, denoted by 'Other' in the plot, are relatively small. In the simulations, the dielectric Rogers RT/duroid® 5880 has $\tan\delta = 9\cdot 10^{-4}$, and the tin-finished copper lines have an effective conductivity of $\sigma \sim 2.6\times 10^{7}\,\mathrm{S/m}$ (measured separately with four-probe method) and surface roughness of $1.3\,\mu\mathrm{m}$. The largest loss contribution arises from the feeding network, which incurs in approximately 3.43–5.51 dB of conductor loss and 0.28–0.63 dB of dielectric loss in the band 3–6 GHz. The feed-line length from the SMA to the different feeding points of the array averages $13.4\lambda_{\mathrm{eff,max}}$, where $\lambda_{\mathrm{eff,max}}$ is the effective wavelength at the lowest frequency of an average-width microstrip line. This average line has an attenuation constant of $\alpha \approx 0.27\ \mathrm{dB}/\lambda_{\mathrm{eff,max}}$, from which conductor and dielectric contributions can be distinguished to be $0.25\ \mathrm{dB}/\lambda_{\mathrm{eff,max}}$ and $0.02\ \mathrm{dB}/\lambda_{\mathrm{eff,max}}$, respectively.

Lastly, the coupling to a prospective quasi-optical system is characterized with the measured fields as explained in Section II. Fig. 14 compares the simulated efficiency (shown earlier in Fig. 10) with the measured one. The results are in good agreement with the simulations.

A. THz Scalability

The choice of the dielectric substrate Rogers RT/duroid® 5880 ($\varepsilon_r \approx 2.2$, $\tan\delta \approx 9\cdot 10^{-4}$, $t_{\mathrm{die}} = 381\,\mu\mathrm{m}$) for the prototypes is motivated by having a comparable dissipation factor as that of Plasma-Enhanced Chemical Vapor Deposition (PECVD) amorphous silicon (a-Si) at 350 GHz ($\varepsilon_r \approx 10$, $\tan\delta \approx 2\cdot 10^{-4}$, $t_{\mathrm{die}} = 300\,\mathrm{nm}$) [17]. Although the electrical thickness and the permittivity are different in the two cases, this has a negligible influence on the radiated fields. Moreover, even if they were the same, the kinetic inductance of the superconducting microstrips would drastically increase the effective propagation constant and the characteristic impedance of the lines, compared to the same line made of a normal conductor. On the other hand, the comparable $\tan\delta$ allows to make a fair comparison in terms of losses per effective wavelength.

A superconducting THz antenna would have negligible conductor loss and would be dominated by the dielectric loss in the feeding network. A separate THz experiment has reported an attenuation constant of $\alpha \approx 0.007\ \mathrm{dB}/\lambda_{\mathrm{eff}}$ for a superconducting NbTiN microstrip on a-Si, where λ_{eff} is the effective wavelength at 350 GHz [17]. As a result, assuming the same electrical length of the feeding network of $13.4\lambda_{\mathrm{eff}}$, we can expect a dielectric loss of 0.09 dB for the THz superconducting device.

V. Conclusions and Outlook

We presented a reflector feed based on focused connected arrays of slots for efficient and broadband illumination of quasi-optical systems including scanning capabilities. The feeding network of the array synthesizes a near-field focused aperture, approximated by a quadratic phase profile, providing with frequency-stable far fields and thus an aperture efficiency higher than 60% over one octave. A linear phase shift can be added to shift the flash point in the focal plane, and thereby enabling beam-steering from within a focusing system.

Two low frequency prototypes were designed and tested. The coupling to a prospective quasi-optical system was investigated by assuming a parabolic reflector with a focal ratio $f_{\#} = 2$, yielding aperture efficiencies in excess of 60% for the whole 3–6 GHz band and allowing to scan one HPBW at the lowest frequency with a frequency-averaged reflector scan loss of 0.2 dB.

The overall efficiency and bandwidth of the focused connected array is limited by the conductor loss and the space occupation of the feeding network. These limitations can be overcome in a future superconducting THz implementation of this antenna concept thanks to the negligible conductor loss and the electrically narrower trace widths [27].

References

[1] C. A. Fernandes, E. B. Lima, and J. R. Costa, "Broadband integrated lens for illuminating reflector antenna with constant aperture efficiency," *IEEE Trans. Antennas Propag.*, vol. 58, no. 12, pp. 3805–3813, Dec. 2010.

[2] O. Yurduseven, D. Cavallo, and A. Neto, "Wideband dielectric lens antenna with stable radiation patterns fed by coherent array of connected leaky slots," *IEEE Trans. Antennas Propag.*, vol. 62, no. 4, pp. 1895–1902, Apr. 2014.

[3] J. M. Edwards *et al.*, "Dual-polarized sinuous antennas on extended hemispherical silicon lenses," *IEEE Trans. Antennas Propag.*, vol. 60, no. 9, pp. 4082–4091, Sep. 2012.

[4] S. Bruni, A. Neto, and F. Marliani, "The ultrawideband leaky lens antenna," *IEEE Trans. Antennas Propag.*, vol. 55, no. 10, pp. 2642–2653, Oct. 2007.

[5] R. Olsson, P. S. Kildal, and S. Weinreb, "The Eleven antenna: A compact low-profile decade bandwidth dual polarized feed for reflector antennas," *IEEE Trans. Antennas Propag.*, vol. 54, no. 2, pp. 368–375, Feb. 2006.

[6] G. Cortes-Medellin, "Non-planar quasi-self-complementary ultra-wideband feed antenna," *IEEE Trans. Antennas Propag.*, vol. 59, no. 6, pp. 1935–1944, Jun. 2011.

[7] A. Akgiray *et al.*, "Circular quadruple-ridged flared horn achieving near-constant beamwidth over multioctave bandwidth: Design and measurements," *IEEE Trans. Antennas Propag.*, vol. 61, no. 3, pp. 1099–1108, Mar. 2013.

[8] C. Granet *et al.*, "A wide-band 4—12.25 GHz feed system for the Australia Telescope 22m-diameter antenna," in *2019 Int. Conf. Electromagn. Adv. Appl. (ICEAA)*, 2019, pp. 0600–0605.

[9] Z. Ying, A. A. Kishk, and P.-S. Kildal, "Broadband compact horn feed for prime-focus reflectors," *Electron. Lett.*, vol. 31, pp. 1114–1115(1), Jul. 1995.

[10] M. Abbas-Azimi, F. Mazlumi, and F. Behnia, "Design of broadband constant-beamwidth conical corrugated-horn antennas [Antenna Designer's Notebook]," *IEEE Antennas Propag. Mag.*, vol. 51, no. 5, pp. 109–114, Oct. 2009.

[11] B. Lee *et al.*, "Design and characterization of 275–500 GHz corrugated horns and optics for a wideband radio astronomy receiver," in *14th Eur. Conf. Antennas Propag. (EuCAP)*, 2020.

[12] S. O. Dabironezare *et al.*, "Quasi-optical system for the ASTE telescope with 1:3 bandwidth at sub-mm wave," in *44th IRMMW-THz*, Paris, France, Sep. 2019.

[13] P. K. Day *et al.*, "Antenna-coupled microwave kinetic inductance detectors," *Nucl. Instrum. Methods Phys. Res. A*, vol. 559, no. 2, pp. 561–563, Apr. 2006.

[14] P. A. R. Ade *et al.*, "Antenna-coupled TES bolometers used in BICEP2, Keck Array, and SPIDER," *Astrophys. J.*, vol. 812, no. 2, pp. 176–182, Oct. 2015.

[15] J. Sayers *et al.*, "The status of MUSIC: the multiwavelength submillimeter inductance camera," in *Proc. SPIE mm Sub-mm Far-Infrared Detectors Inst. Astron. VII*, vol. 9153, 2014, pp. 57–74.

[16] S. Hähnle *et al.*, "Suppression of radiation loss in high kinetic inductance superconducting co-planar waveguides," *Appl. Phys. Lett.*, vol. 116, no. 18, p. 182601, 2020.

[17] ——, "Superconducting microstrip losses at microwave and submillimeter wavelengths," *Phys. Rev. Applied*, vol. 16, pp. 014 019(1–8), Jul. 2021.

[18] M. W. A.W. Rudge, "New technique for beam steering with fixed parabolic reflectors," *Proc. IEE*, vol. 118, pp. 857–863(6), Jul. 1971.

[19] W. D. Fitzgerald, "Limited electronic scanning with a near-field cassegrainian system," Lincoln Lab., Massachusetts Institute of Technology, Tech. Rep., 1971.

[20] B. Houshmand *et al.*, "Analysis of near-field cassegrain reflector: plane wave versus element-by-element approach," *IEEE Trans. Antennas Propag.*, vol. 38, no. 7, pp. 1010–1017, 1990.

[21] R. C. Hansen, *Phased Array Antennas*. John Wiley & Sons, Ltd, 2009, ch. 14, pp. 503–510.

[22] K. D. Stephan *et al.*, "A near field focused microstrip array for a radiometric temperature sensor," *IEEE Trans. Antennas Propag.*, vol. 55, no. 4, pp. 1199–1203, 2007.

[23] Y. F. Wu, Y. J. Cheng, and Z. X. Huang, "Ka-band near-field-focused 2-D steering antenna array with a focused Rotman lens," *IEEE Trans. Antennas Propag.*, vol. 66, no. 10, pp. 5204–5213, 2018.

[24] M. Ettorre *et al.*, "Experimental validation of Bessel beam generation using an inward Hankel aperture distribution," *IEEE Trans. Antennas Propag.*, vol. 63, no. 6, pp. 2539–2544, 2015.

[25] S. M. Anlage, H. J. Snortland, and M. R. Beasley, "A current controlled variable delay superconducting transmission line," *IEEE Trans. Magn.*, vol. 25, no. 2, pp. 1388–1391, Mar. 1989.

[26] J. Bueno *et al.*, "Full characterisation of a background limited antenna coupled KID over an octave of bandwidth for THz radiation," *Appl. Phys. Lett.*, vol. 110, no. 23, pp. 233 503(1–5), Jun. 2017.

[27] D. J. Thoen *et al.*, "Combining UV-and electron-beam lithography for superconducting bandpass filters in mm/sub-mm astronomy," in *Proc. SPIE mm Sub-mm Far-Infrared Detectors Inst. Astron. X*, vol. 11453, Dec. 2020.

[28] J. W. Sherman, III, "Properties of focused apertures in the Fresnel region," *IRE Trans. Antennas Propag.*, vol. 10, no. 4, pp. 399–408, Jul. 1962.

[29] R. C. Hansen, "Focal region characteristics of focused array antennas," *IEEE Trans. Antennas Propag.*, vol. 33, no. 12, pp. 1328–1337, Dec. 1985.

[30] J. Ruze, "Lateral-feed displacement in a paraboloid," *IEEE Trans. Antennas Propag.*, vol. 13, no. 5, pp. 660–665, Sep. 1965.

[31] D. Cavallo and A. Neto, "A connected array of slots supporting broadband leaky waves," *IEEE Trans. Antennas Propag.*, vol. 61, no. 4, pp. 1986–1994, Apr. 2013.

[32] D. Cavallo, W. H. Syed, and A. Neto, "A 5:1 connected slot array loaded with artificial dielectric layers," in *Proc. IEEE Int. Symp. Phased Array Syst. Technol. (PAST)*, Waltham, MA, US, Oct. 2016.

[33] D. Paris, W. Leach, and E. Joy, "Basic theory of probe-compensated near-field measurements," *IEEE Trans. Antennas Propag.*, vol. 26, no. 3, pp. 373–379, May 1978.

[34] E. Gandini *et al.*, "Wide field of view inversely magnified dual-lens for near-field submillimeter wavelength imagers," *IEEE Trans. Antennas Propag.*, vol. 66, no. 2, pp. 541–549, Feb. 2018.